ELSEVIER

Chemical Engineering Journal 135S (2008) S46–S56

Chemical Engineering Journal

www.elsevier.com/locate/cej

Understanding thermal integration issues and heat loss pathways in a planar microscale fuel processor: Demonstration of an integrated silicon microreactor-based methanol steam reformer

Keyur Shah, R.S. Besser *

New Jersey Center for Microchemical Systems, Department of Chemical, Biomedical and Material Engineering, Stevens Institute of Technology, Castle Point on Hudson, Hoboken, NJ 07030, United States

Abstract

Methanol reforming offers an attractive source of hydrogen for proton exchange membrane fuel cell (PEMFC) systems for portable power. At present, the greatest obstacle to realization of these systems is the extraction of hydrogen from the hydrocarbon fuel, i.e., the fuel processing part. Because of size and portability, microchemical technology has shown assuring results in the field of fuel processing. However, several roadblocks persist in the development of an integrated micro-fuel processor and fuel cell system. Thermal management in miniature systems is perhaps the most crucial of these challenges. In this study, a silicon microreactor-based catalytic methanol steam reforming reactor was demonstrated in the context of complete thermal integration to understand this critical issue. Detailed experiments were carried out to quantify heat losses through various pathways from the planar microreactor structure. Based on these experiments, an empirical correlation is developed to predict natural convection heat transfer coefficient from meso to microscale devices. The result provides fundamental insight of critical thermal issues such as transfer of heat between reactor components, control of temperature, insulation, and heat losses. Based on this understanding, suggestions are made for scale up of reactor components and a packaging scheme for reduction of convective and radiative losses.

Keywords: Portable power; PEM fuel cell; Microreactor; Fuel processing; Methanol reformer; Thermal management

1. Introduction

Fuel cell technology is a promising means of transferring chemical energy to electrical energy [1]. Recently, there has been great interest in the development of microscale fuel cell systems for portable power generation, as prominent alternatives to batteries. The proton exchange membrane fuel cell (PEMFC) is particularly attractive and promising for portable applications because of its simplicity in design and operation, mild operating conditions, and ability to provide high power density and nearly instant power [1,2]. However, the success of PEMFC technology for portable power depends heavily on the development of an efficient means of delivering the appropriate fuel to the cell.

Generating pure hydrogen by processing easily stored liquid fuels represents an attractive source of hydrogen [3,4]. Fuel processing adds complexity, weight, and cost compared to the direct fuel cell or a system running directly on hydrogen, however the effective energy storage density is significantly higher. Liquid hydrocarbons offer strong possibilities as an energy source for portable power systems if an efficient, lightweight, and compact fuel processor can be developed and integrated with a PEMFC system.

Methanol is the fuel of choice for portable power applications, offering high hydrogen–carbon ratio, high energy density (5600 Wh/kg), ready availability, and low boiling point [5]. Moreover, methanol is sulfur free and it can be reformed relatively easily at low temperatures (250–300 °C), simplifying the micro-fuel processor design. Fig. 1 shows steps for processing of methanol to produce a hydrogen-rich gas suitable for a low temperature (70–80 °C) PEMFC.

The steam reforming (SR) reaction is highly endothermic in nature and thus requires external energy. This energy can be reasonably obtained by combusting excess hydrogen from the anode exhaust of the fuel cell. A relatively low CO concentration of 1–2% is attained while operating the reformer at temperatures ranging from 220 to 260 °C as a consequence of reaction thermodynamics [6–8]. Therefore, a methanol-based fuel processing system must include a CO clean up step like preferential

* Corresponding author. Tel.: +1 201 216 5257; fax: +1 201 216 8306.
E-mail address: rbesser@stevens.edu (R.S. Besser).

1385-8947/$ – see front matter © 2007 Elsevier B.V. All rights reserved.
doi:10.1016/j.cej.2007.07.044

Nomenclature

A	surface area (m^2)
A_w	cross-sectional area of the wire (m^2)
E	emissive power (W/m^2)
$E_{b\lambda}$	spectral blackbody emissive power ($W/(m^2\ \mu m)$)
h	heat transfer coefficient ($W/(m^2\ K)$)
I	current (A)
I_λ	radiative intensity ($W/(m^2\ sr)$)
k_λ^{Si}	spectral absorption coefficient of silicon (m^{-1})
k_λ^{py}	spectral absorption coefficient of Pyrex (m^{-1})
l	length of the wire (m)
N_{Nu}	Nusselt number
N_{Ra}	Rayleigh number
P'	perimeter of the wire (m)
Q_{conv}	heat loss by convection
Q_{in}	heat input (W)
Q_{loss}	total heat loss (W)
Q_{rad}	heat loss by radiation
Q_{wires}	heat loss from the attached wires
T_s	surface temperature (K)
T_∞	ambient temperature (K)
V	voltage (V)

oxidation (PrOx), as this relatively low level of CO is still sufficient to poison the PEMFC catalyst.

1.1. Microchemical systems for microscale fuel processing

Microchemical systems are well-suited to small-scale power generation as they enable integration and stacking of miniature fuel processor and fuel cell components with the fuel delivery system for compact, lightweight power generation [9]. The small footprints of microreactors and their peripherals make them well-suited for all critical components of a fuel processor like the combustor, SR, PrOx reactors, etc. Their microscale dimensions result in extremely small heat and mass transport resistances [10], making them efficient in applications where it is necessary to thermally couple highly endothermic and exothermic processes.

2. Thermal management in microscale fuel processing

Considerable efforts have been made to develop an integrated portable fuel processor/fuel cell system, however, several issues

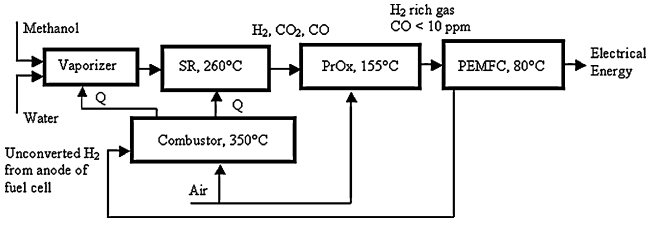

Fig. 1. Processing steps required for generating high purity hydrogen from methanol.

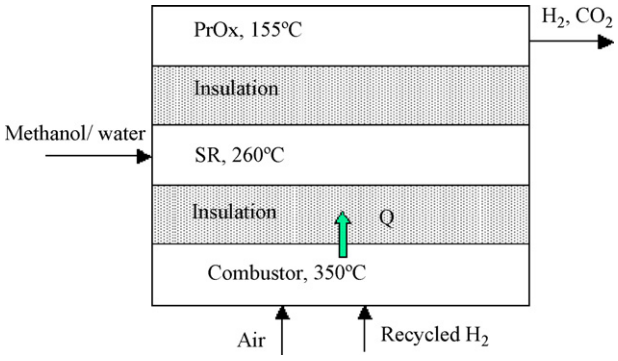

Fig. 2. Integration of fuel processing components.

and challenges persist. Based on the literature and our own research, several of these key issues are identified and discussed in our previous paper [11].

Thermal management in miniature systems is perhaps the most crucial challenge for microscale fuel processors. The fuel processor needs effective thermal coupling to allow transfer of energy from the heat-producing combustor to the endothermic SR. Coupling endothermic and exothermic components of the fuel processor and minimizing losses promotes a high thermal efficiency. However, such coupling must be accomplished in a manner that permits the maintenance of specific temperatures in the various components as shown in Fig. 2 and maintains the surface of the package near room temperature. Microreactors generally offer high heat transfer rates mainly because of high surface-to-volume ratio and short conduction paths. This characteristic results in efficient heat extraction but at the same time results in higher heat losses to the ambient. Therefore, thermal management offers a dual challenge of opposing the heat losses from the system that arise from high surface-to-volume ratio in conjunction with maintaining temperature gradients within the system to allow desired conditions in the unit reaction steps.

Different materials are being used for the construction of microscale fuel processing components [12–19]. However, all the materials approaches are confronted with the thermal management issues described above. Because of the nature of microfabrication processes, all these approaches employ flat and sheet-like reactor elements or short multilayer stacks of these sheet-like devices. This kind of low aspect ratio, planar architecture offers an excellent inter-component heat transfer, however, it is poor for heat retention and results in significant heat losses to the ambient.

3. Understanding thermal management issues: demonstration of an integrated SR

To address the crucial issue of heat management, with a focus on the SR as the most critical component of the fuel processor, a silicon microreactor-based SR was designed, fabricated, and demonstrated in the context of thermal integration reflective of an overall fuel processor. An integrated design (Fig. 3) was made where thin metal film heaters, temperature sensors, and microfabricated insulation were directly embedded into the unit. External heat is introduced to simulate integration with

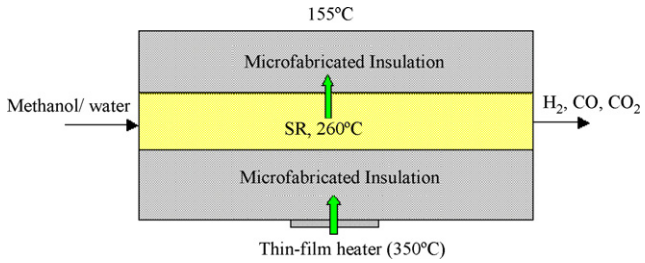

Fig. 3. Demonstration of thermally integrated SR.

a combustor by controlled heat introduction. Detailed thermal data (heat input required, heat losses, temperature profiles) and reaction data (conversion and selectivity) were acquired.

Because of its various advantages, silicon microfabrication technology was employed in this work to achieve miniaturization. However, our intent is to perform thermal and reaction experiments whose outcome depends most critically on microscale geometry and less so on the materials of construction. In this way the results obtained may be generalizable to any of the materials technologies.

3.1. Design of micro-methanol SR

A silicon microreactor with a reaction zone of 1 cm × 1 cm × 400 μm (0.04 cm^3) was designed. The reaction zone was designed to incorporate a packed bed of commercial copper-based powder catalyst. The microreactor consisted of an inlet to introduce the mixture of vaporized methanol and steam, an outlet to remove reformate, a packed bed reaction zone, a flow manifold structure, and filter structures at the outlet to trap catalyst particles.

3.2. Internal heat management: thermal coupling and design of insulation

In order to maintain desired temperature gradients between fuel processor components, insulators are required to bridge the temperature differences. We found that the selection of insulation is critical to thermal integration. The goal was to design insulation such that it does not add much to the weight and volume of the total system and can be easily integrated using microfabrication processes. Because of the high thermal conductivity of silicon, short conduction paths, and the high surface-to-volume ratio inherent to microreactors, only insulating materials that can offer ultra-low thermal conductivity can be effective to bridge these temperature differences and to minimize conductive and convective heat losses to the surroundings.

The best commercial insulators have thermal conductivities in the range of 0.02 W/(m K) and are difficult to integrate into a microfabricated unit. However, vacuum packaging of microreactors can provide an effective means of insulation. From the kinetic theory of gases, it is known that the thermal conductivity of a gas is approximately independent of pressure for atmosphere and above [20], and decreases with sub-atmospheric pressures, as the mean free path becomes less than the enclosure dimensions [21]. Fig. 4 shows a plot of k_p/k_0 (k_p being thermal conductivity of air at sub-atmospheric pressure [22] and k_0 being thermal conductivity of air at atmospheric pressure) versus sub-atmospheric pressures for a cavity depth of 500 μm. A microfabricated cavity surrounding the reactor filled with low-pressure gas offers low thermal conductivity down to approximately 0.001 W/(m K). Silicon microfabrication enables a straightforward approach to this structure, as the cavity etched in silicon can be sealed to trap the desired vacuum and the desired residual gas species.

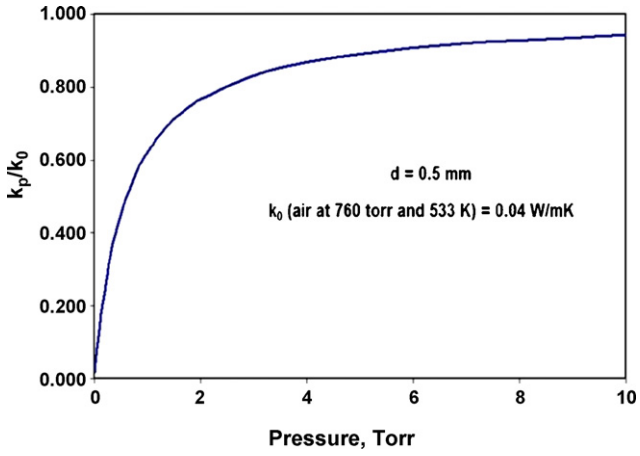

Fig. 4. Thermal conductivity of air at sub-atmospheric pressures for a cavity depth of 500 μm.

3D thermal simulation using ANSYS® simulation software was carried out to design microfabricated vacuum insulation such that it can maintain the required temperature gradients. The simulation also determined placement of the combustor and PrOx zones in reference to the reformer reaction zone, pressure in the cavity and the depth of cavity required. The reforming microreactor was designed to produce 3.84e−4 mol min^{-1} of hydrogen. Considering 75% hydrogen utilization in the fuel cell, the remaining 9.6e−5 mol min^{-1} of hydrogen in the fuel cell anode effluent when burned, gives 0.38 W based on the lower heating value (LHV) of hydrogen. The temperature boundary condition at PrOx side, endothermic heat of reforming reaction, reactant and product sensible heats used in the 3D thermal model are shown in Fig. 5(a) while Fig. 5(b) shows the simulation result. The simulation yielded the required temperature distributions in the combustor and SR compartments at fixed temperature boundary condition of 155 °C at PrOx side. For generality, the model did not consider heat losses.

3.3. Design and fabrication of an integrated SR

The design to simulate an integrated SR is shown in Fig. 6(a). The stack of six chips consisted of insulation chips surrounding the reforming microreactor. The silicon microreactor was covered with a Pyrex™ cover on the top. Thin-film resistance temperature detector (RTD) type temperature sensors were patterned at different positions on the backside of the silicon microreactor. Three temperature sensors were placed at different positions to measure the reaction zone temperature distribution and one each was placed at the inlet and outlet section as shown

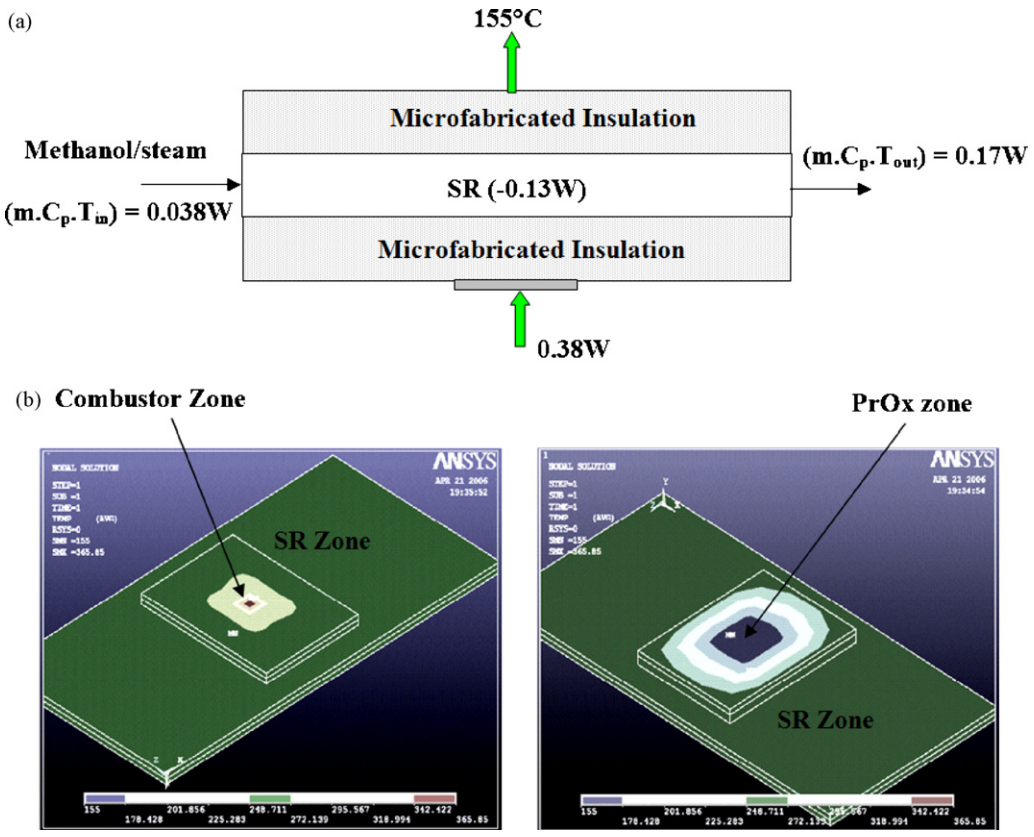

Fig. 5. (a) The concept of 3D thermal model used to design microfabricated vacuum insulation. (b) 3D thermal simulation results showing the temperature distribution in different compartments.

in the superimposed image (Fig. 6(b)) of the front and backside CAD masks of the microreactor. The sensors had meandering resistors with a 4-wire design to minimize lead resistance effects. The insulation consisted of an assembly of silicon and glass chips. The silicon chip had a cavity in the center and was bonded with the Pyrex™ heater and temperature sensor substrate as shown in the superimposed image of the mask designs of silicon and glass chips in Fig. 6(c). The insulation requirements, described next, were determined based on thermal and structural considerations.

The insulation requirement between the combustor and the reformer was not demanding, as the reformer needs endothermic heat of reaction. An appropriate thermal conductivity and insulating thickness was obtained in this case by a 50-μm deep cavity containing air at atmospheric pressure. The lateral dimensions of the silicon and glass were 1.2 cm × 1.5 cm while the cavity was slightly smaller at 1.0 cm × 1.3 cm. The combustor is 2.8 mm × 2.8 mm and is centered over an insulation chip. An integrated on-chip thin-film Pt heater meandering along this area was used to simulate the combustor. Three thin-film temperature sensors were also patterned on the glass chip. One sensor was located directly in the center of the combustor zone, while two others were placed on either side at a distance of 600 μm from the center.

On the opposite side of the assembly, more stringent thermal isolation was required between the reformer and the PrOx. For this reason, the insulation between the reformer and the PrOx had a 200-μm deep cavity and was sealed with vacuum of less than 5 mTorr. The silicon insulation chip of lateral dimensions 1.2 cm × 1.5 cm had a cavity of 1.1 cm × 1.4 cm. As determined from the ANSYS® thermal simulation, the effective insulation in this case required higher vacuum, a deeper cavity, and smaller conductive distance between the cavity and the insulation chip. Since silicon has a high thermal conductivity (150 W/(m K)), only a 500-μm wide border was maintained around the cavity on the silicon insulation chip to minimize vertical conduction of heat.

Silicon microfabrication technology was used to fabricate components of the integrated device. Fig. 7 shows the fabricated components of an integrated SR.

3.4. Incorporation of commercial catalyst and assembly of an integrated SR

The commercial BASF catalyst is incorporated in the form of a packed bed in the silicon microreactor bonded with glass. The catalyst was received in a pellet form, and was ball milled and sieved to obtain catalyst particles of mean diameter 70–80 μm. These particles were then introduced into the reaction zone through the inlet via while creating suction at the outlet. The reactor has an array of catalyst filter structures at the outlet with a gap spacing of 30 μm ensuring that catalyst particles larger than this remain trapped within the reaction zone. Fig. 7(c) shows the silicon microreactor packed with incorporated catalyst.

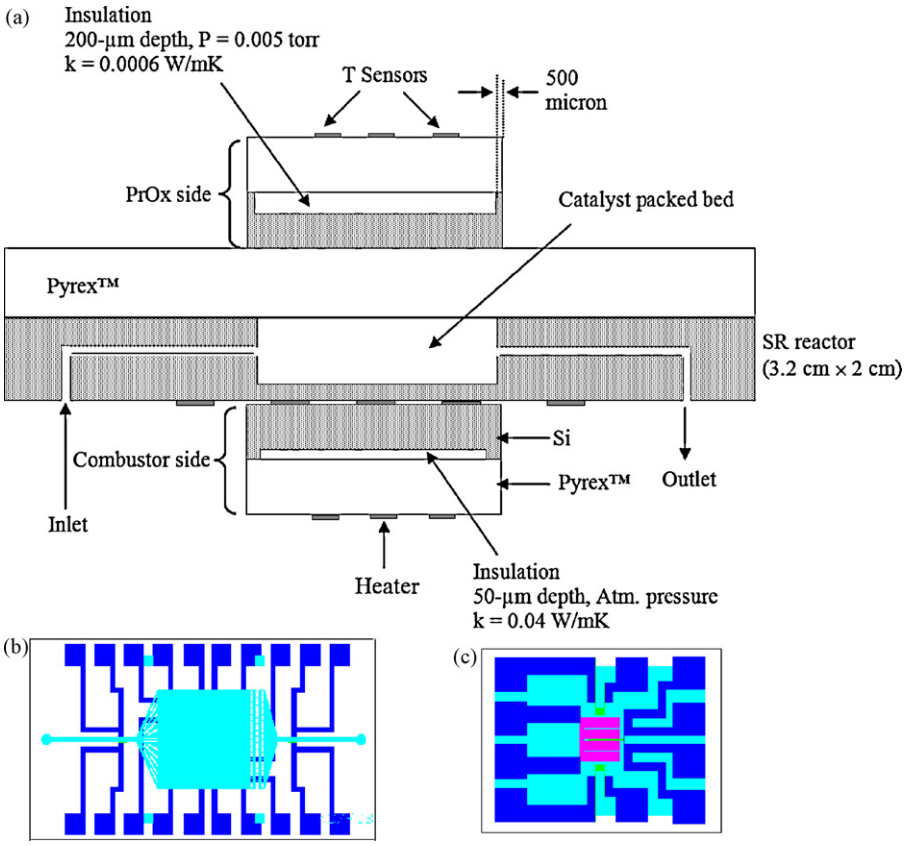

Fig. 6. (a) The design of the integrated SR. (b) Superimposed image of the front and backside CAD masks of the microreactor. (c) Mask design for silicon and glass chips of the insulation layer. Silicon chip with cavity to be etched in the center and glass chip patterned with thin-film heater and temperature sensors.

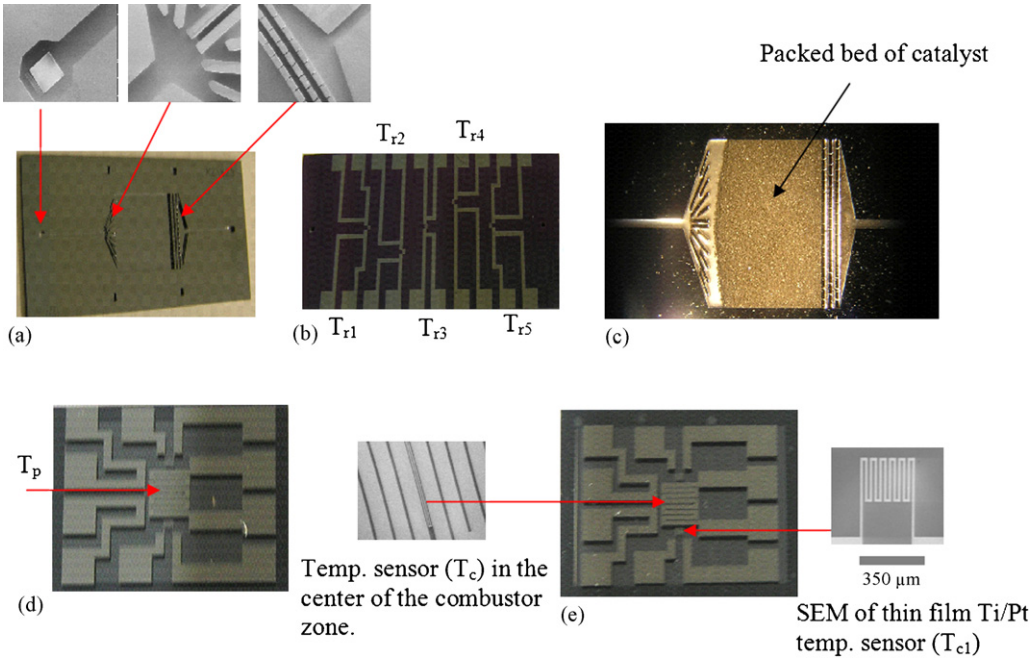

Fig. 7. (a) Frontside of silicon SR microreactor with SEM images of inlet via, flow manifold, and catalyst traps. (b) Backside of SR microreactor showing patterned temperature sensors. (c) Incorporation of catalyst in the form of packed bed by vacuum loading. Catalyst loading achieved was 53.1 mg. (d) PrOx side insulation chips. Etched cavity in silicon bonded under vacuum with patterned glass. (e) Combustor side insulation chips with SEM images of central combustor (heater) zone and temperature sensors.

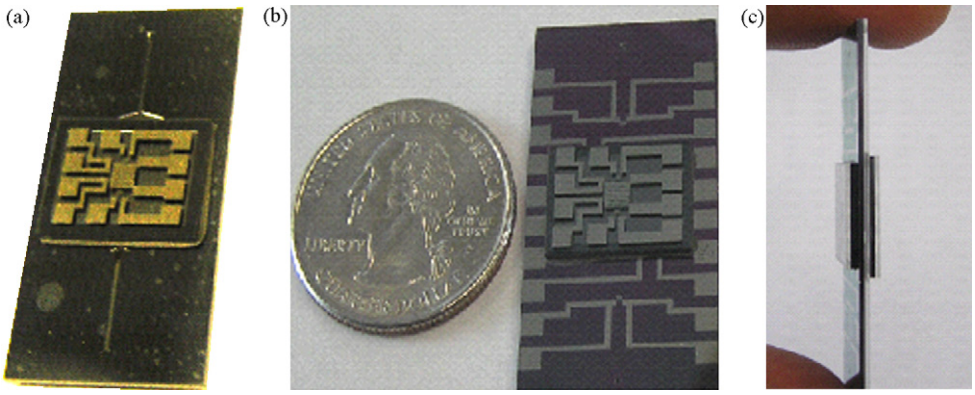

Fig. 8. SR microreactor bonded with the insulation chips. (a) Frontside of SR microreactor bonded with insulation chips. (b) Backside of reactor bonded with insulation chips. (c) Assembled integrated microreformer (six-chip stack).

Next, the insulation chips are bonded on the front and back sides of the catalyst-loaded microreactor using high temperature epoxy. Fig. 8 shows the microreactor bonded with the insulation chips.

4. Results and discussion

4.1. Thermal characterization

Thermal characterization was carried out without flows in order to measure critical thermal parameters including heat requirement, heat transfer rates between components, lateral and vertical temperature distributions, insulation effectiveness, and heat loss mechanisms.

Electrical connections were made by attaching thin wires to the contact pads with conductive silver epoxy. All thin-film temperature sensors were first calibrated to relate the change in resistance with temperature. A linear trend was observed by plotting normalized resistance (R/R_0) versus the temperature. The temperature coefficient of resistance (TCR) was then calculated using a linear fit, which allowed estimating temperatures from the experimental resistance data.

During thermal characterization, the integrated device was not supported by any fixture to avoid external thermal contact. Instead, the device was made to rest on the attached wires and kept suspended in air as shown in Fig. 9.

For characterization, electrical heating with the integrated thin-film heater was carried out to introduce a well-defined energy input. Heating in air was carried out until the required 260 °C temperature was obtained in the SR reaction zone. Once the device reached steady state, the current and voltage across the heater were measured along with resistances of temperature sensors using digital multimeters. The heat required to raise the temperature of the reaction zone and corresponding temperatures of each component were thus obtained. We could introduce close to 6.8 W using this integrated thin-film heater. With this power, it was only possible to obtain a temperature of 230 °C in the reforming reaction zone because of the high heat losses. We observed that putting more power than ≈6.8 W resulted in a short circuit of the heater resistor and cracks in glass possibly resulting from the combined effect of high current density and

Fig. 9. Thermal characterization of an integrated device suspended in air.

high temperature within the small heater zone. Fig. 10 shows the temperatures of different components of the integrated device as a function of the power input to the heater.

Despite the losses, it was possible to obtain the required thermal isolation between the combustor, the reformer and the PrOx units. For the reformer temperature of 230 °C, the temperature

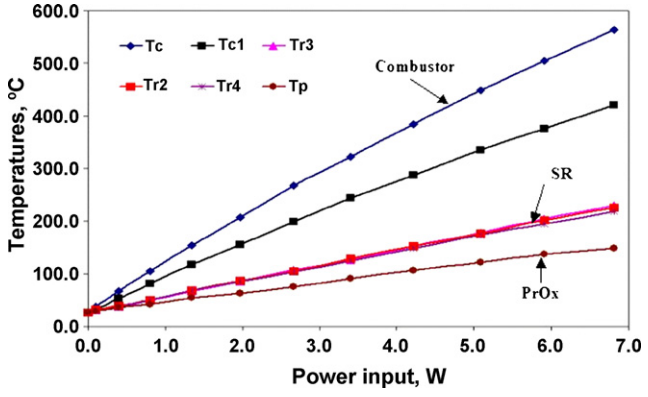

Fig. 10. Temperature obtained in different components vs. the power input to the uninsulated integrated device suspended in the ambient.

obtained in the combustor and the PrOx were 564 and 150 °C, respectively. The integrated device was design to obtain 350 and 155 °C in the combustor and PrOx, respectively, for the reformer temperature of 260 °C. The reaction zone remained at uniform temperature as measured by three temperature sensors (Tr_2, Tr_3, Tr_4) placed at different location on the backside of reaction zone. This was due to the high thermal conductivity of the silicon embedded between the insulation chips.

However, for the other free surfaces open to the ambient, large lateral thermal gradients were observed even from these small-scale devices. For example, we observed a temperature difference of greater than 100 °C between a combustor (T_c, measured by a thin-film sensor placed in the center of the combustor) and T_{c1}, thin-film temperature sensor that was placed 600 μm from the combustor. Therefore, it was necessary to measure the surface temperature distributions at even higher resolution than originally planned. In addition to thin-film temperature sensors, manually placed thermocouples were used to obtain temperatures at locations intermediate to the micro-RTD sensors.

The individual contributions of the different heat loss pathways was determined from the measured heat input as a function of surface temperature. We make the normal assumption that heat is lost from the free surfaces by free convection and radiation. In addition to this, conduction through attached suspending wires and thermocouples was considered. Therefore, at steady state,

$$Q_{in} = VI = Q_{loss} = Q_{wires} + Q_{conv} + Q_{rad} \quad (1)$$

Heat loss from these wires on each surface was estimated by applying the so-called pin fin theory [23]. Heat dissipated from the wires was calculated by integrating the loss over the side surface of the wires, yielding

$$Q_{wires} = (hP'(T_s - T_\infty)\tanh \alpha l)\frac{n}{\alpha} \quad (2)$$

where $\alpha = hP'/kA_w$, $P' = 2\pi R$, is the perimeter of the wire, R the radius of the wire (250 μm), A_w the cross-sectional area of the wire, h the heat transfer coefficient = 50 W(m^2 K) (assumed), T_s the edge temperature of the respective surface, T_∞ the ambient temperature, l = 10 cm, the length of wire, and n is the number of wires on each free surface.

Since the substrate media incorporated here are transparent to significant portions of the emission spectrum involved, the spectral volumetric emission and absorption in silicon and glass were taken into account. For an isothermal, absorbing and emitting medium, the intensity $I_\lambda(L)$ of a monochromatic beam of radiation is given by the following equation [24]:

$$I_\lambda(L) = I_\lambda(o)\,e^{-k_\lambda L} + I_{b\lambda}(1 - e^{-k_\lambda L}) \quad (3)$$

The first term, $I_\lambda(o)\,e^{-k_\lambda L}$, relates to the intensity of an impinging beam and its reduction within the solid medium of thickness L due to absorption. The second term, $I_{b\lambda}(1 - e^{-k_\lambda L})$, is the volume-generated emission taking place over the thickness of material, L. For a composite of adjacent silicon and glass pieces of thickness L and L', respectively, Eq. (3) then can be used to determine intensity at the free surfaces of the composite. Eq. (4),

$$I_\lambda(L') = I_{b\lambda}(1 - e^{-((k_\lambda^{Si}L/2) + k_\lambda^{py}L')}) \quad (4)$$

gives the intensity at the free surface of the Pyrex piece in a composite of silicon and Pyrex. This equation can also be rewritten to obtain the intensity $I_\lambda(L)$ from the free surface of the silicon piece. In these equations, $I_{b\lambda} = E_{b\lambda}/\pi$, where $E_{b\lambda}$ is the spectral blackbody emissive power (W/(m^2 μm)) [20]. k_λ^{Si} and k_λ^{py} are the spectral absorption coefficients of silicon and Pyrex, respectively. These calculations are made for the wavelength range from 0.1 to 100 μm to obtain the total emissive power E (W/m^2), which is then multiplied by area to obtain Q_{rad}. After determination of the radiation rate, the estimated values of Q_{wires} and Q_{rad} were then subtracted from the measured heat loss to evaluate Q_{conv} as in Eq. (5).

$$Q_{conv} = Q_{loss} - Q_{wires} - Q_{rad} \quad (5)$$

Fig. 11 shows the steady-state heat loss due to conduction through wires, natural convection, and radiation as a function of SR reaction zone temperature. The heat loss estimate shows that the surface heat loss by what we initially considered to be natural convection makes up the major fraction of overall heat loss at atmospheric pressure.

An unexpected finding from these results is that the effective convective losses were found to be significantly higher at this length scale than the predictions obtained by correlations for objects of conventional scale. We found that the heat transfer coefficient increases dramatically as the surface dimensions decrease and was severely underpredicted in our initial estimates which relied on standard correlations. Based on additional experiments and analysis, we developed the following dimensionless correlation to predict the heat transfer coefficient of natural convection for micro to mesoscale objects (sub-mm to mm scale).

$$N_{Nu} = 1.7N_{Ra}^{0.08} \quad (6)$$

where N_{Nu} is the Nusselt number and N_{Ra} is the Rayleigh number. The uncertainty in predicting Nusselt numbers from these

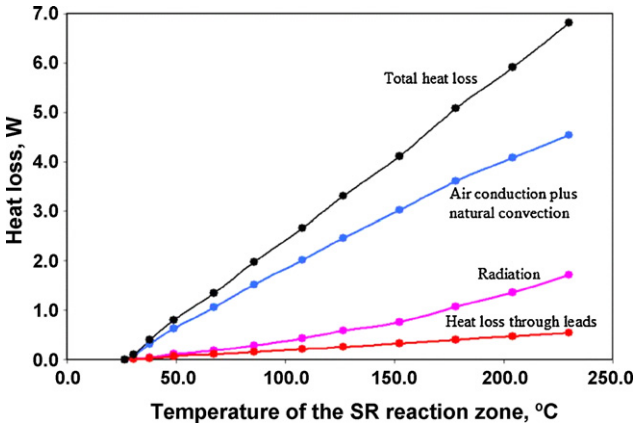

Fig. 11. Total steady-state heat loss measured experimentally and estimated heat loss by various pathways vs. the SR reaction zone temperatures. Curve labeled "natural convection" includes loss via gas phase conduction in adjacent air.

correlations is approximately ±15% attributed mainly to experimental error and assumptions made during estimation of the different losses.

The high convective losses from planar surface to the ambient are believed to be the combined effect of air conduction and natural convection with the former dominating at this scale. When we compared the convective heat rate using a conventional, macroscale correlation from the literature [20], we found that it could only account for 30% of the effective convection rate. This is in agreement with the results of others who found extraordinarily high effective rates of convection from mm- to cm-scale surfaces [25,26], leading to suggestions that direct conduction in the air is responsible for the discrepancy. We adhere to this hypothesis as well, and hence the correlation we developed (Eq. (6)) conveys an effective convection coefficient, since we believe another process besides convection must be contributing. Gas-phase (air) conduction could be explained as significant as system size decreases in the following way: the small volume of gas heated by a small (mm- to cm-scale) interfacial area is changed in density due to an increase in temperature. While with macroscale objects, this density difference drives the flows associated with natural convection, the buoyancy forces on the small volumes of heated gas in this case are too small to strongly overcome the forces of viscous drag which oppose the convective motion. As a result, the gas does not flow significantly, and direct conduction from the surface becomes dominant.

Heat loss by radiation is also important in the consideration of our measurements as it amounts to a significant fraction of the total heat loss especially at high temperature. However, in all of the conditions measured, radiation rates were lower than the corresponding rates of effective convection (combined air conduction and convection). For all temperatures measured, conduction loss to the attached wires was less than 7%.

Thermal characterization of this assembled device was then carried out under vacuum to determine the effect of sub-atmospheric pressure on steady-state heat loss. The integrated device resting on the attached wires was placed in the vacuum chamber. The chamber was evacuated to 50 mTorr, and the steady-state heat losses were characterized as a function of surface temperatures (Fig. 12). Fig. 13 shows the temperature obtained in different compartments as a function of the power input to the heater.

Thermal measurements under vacuum required ≈4.3 W of heat in order to obtain the required 260 °C temperatures in the SR reaction zone. The steady-state heat loss data was then analyzed to determine relative magnitudes of conduction through wires, air conduction plus natural convection, and radiation losses. Fig. 14 shows the comparison of heat losses by air conduction plus natural convection as a function of SR reaction zone temperature for the ambient pressure and vacuum tests. For the SR reaction zone temperature of 230 °C, the heat loss by air conduction plus natural convection was 2.1 W under vacuum compared to 4.8 W observed at ambient pressure. Therefore, it was possible to reduce this loss by about 60%. However, even at this level of vacuum, the convection could not be entirely suppressed.

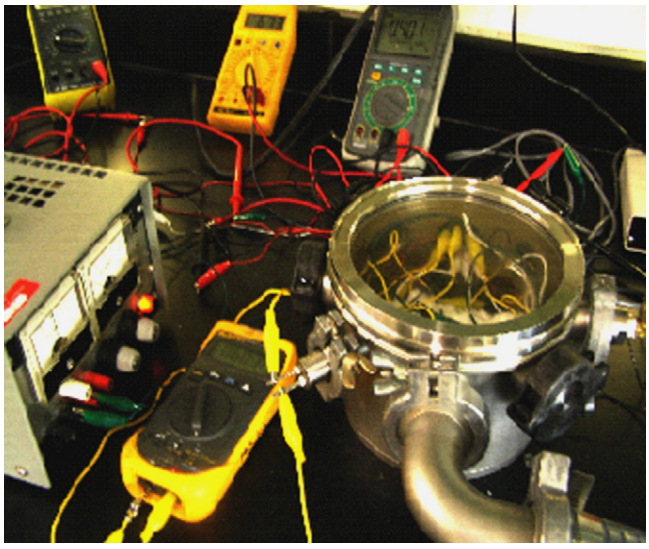

Fig. 12. Thermal characterization of the integrated device suspended in vacuum chamber.

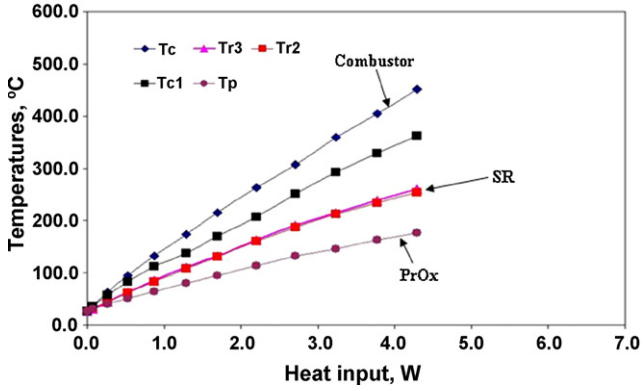

Fig. 13. Temperature obtained in different components vs. the power input for the integrated device suspended in vacuum chamber.

Additional thermal characterization experiments were carried out both at atmospheric pressure and under vacuum where the integrated device was covered in commercial fiberglass insulation (Fig. 15). Table 1 shows the heat input, temperatures

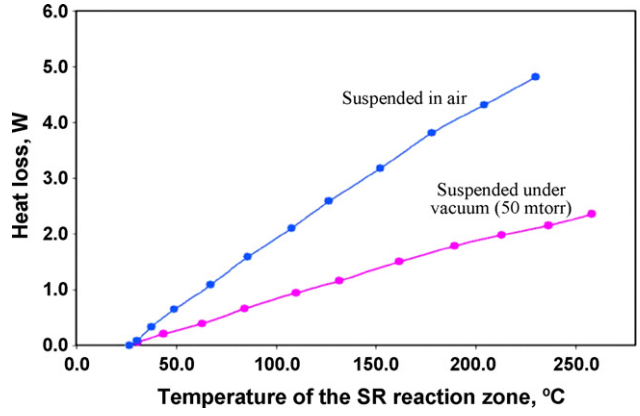

Fig. 14. Heat loss by air conduction and natural convection as a function of the SR reaction zone temperature for the integrated device suspended in air and under vacuum.

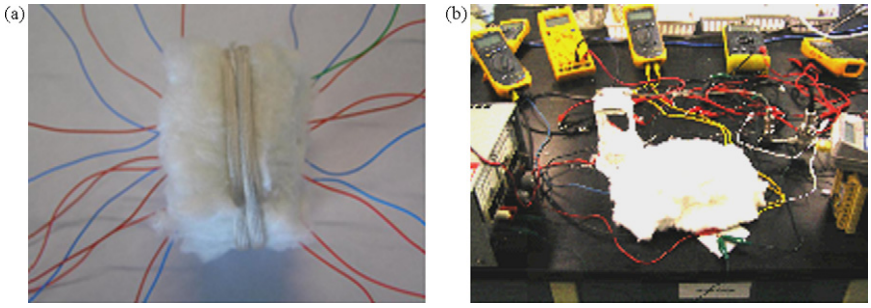

Fig. 15. (a) Integrated device covered both sides with fiberglass insulation of size 4 cm × 2.3 cm × 2.4 cm. (b) Integrated device placed in a 10 cm × 8 cm × 8 cm of insulation.

obtained in combustor, SR, and PrOx zones, and breakdown of steady-state heat loss into convective and radiative losses for each experiment.

As shown in Table 1, the device covered in loosely packed fiberglass insulation showed the best performance at both atmospheric and vacuum tests. The heat losses decrease with an increase in thickness of the insulation, resulting from reduced temperature gradients and heat transfer coefficients. However, using a large amount of insulation adds to the weight and especially the volume of the overall system, which lead to reductions in energy density.

4.2. Reaction characterization

Experiments are carried out to determine conversion and selectivity, hydrogen production rate (corresponding power output), heat required to drive the reforming reaction, and thermal effects on reaction.

The reaction was carried out at different temperatures from 220 to 280 °C with a combined feed flow rate of 0.009 ml min^{-1} (methanol flow rate of 1.36e−4 mol min^{-1}). At 280 °C, close to 100% methanol conversion was achieved, producing 9 sccm of H_2. At the reaction temperature of 220 °C, the methanol conversion was decreased to 50%, reducing the H_2 produced to 5.2 sccm. CO was not formed in detectable amounts at the reaction temperature of 220 °C, however, it increased to 1.1% as the temperature increased to 280 °C.

The effect of feed flow rate on the methanol conversion was determined by changing combined feed flows from 0.007 to 0.015 ml min^{-1} at a reaction temperature of 260 °C. Methanol conversion was decreased, while the reformate and hydrogen flow rates increased with increasing feed flow rate (resulting in decreasing residence time). With the total feed rate of 0.015 ml min^{-1}, 82% of methanol conversion was achieved, producing 14.3 sccm of hydrogen. Considering 60% efficiency and 75% H_2 utilization, this stream is sufficient to produce 1.04 W from the fuel cell.

We did not observe any major change in temperature profiles during the reaction arising from the flows and endothermic natural of the reaction. This is because the heat required to carry out the endothermic SR reaction is quite small relative to the amount of heat to be input (because of high heat losses) in order to achieve the required reaction temperature.

4.3. Packaging suggestions and scale up

Based on the understanding gained from thermal characterization experiments, the following packaging suggestions are made to reduce air conduction, convection, and radiation losses.

- In scaling up, it is desirable to form a stacked three-dimensional assembly in preference to using larger chips (3D architecture instead of planar sheets). This reduces the surface-to-volume ratio and thus the surface convective and radiative losses.
- Heat losses by air conduction and natural convection constitute a significant fraction of total heat loss at ambient pressure. These heat losses were reduced by covering the device in insulation and operating under vacuum. Use of low-*k* insulating materials helps reduce these losses. However, there is a trade-

Table 1
Heat required to raise reformer temperature to 260 °C, corresponding to temperatures obtained in the combustor, SR, and PrOx zones, and breakdown of steady-state heat loss into convective and radiative losses for each experiment

Experiment	Q_{in} (W)	T_{comb} (°C)	T_{SR} (°C)	T_{PrOx} (°C)	Q_{conv} (W)	Q_{rad} (W)
Suspended on wires in ambient (Fig. 10)	6.8	564	230	149	4.8	1.7
Suspended on wires under vacuum (Fig. 13)	4.3	452	260	176	2.4	1.7
Covered with fiberglass insulation of size $l = 4$ cm, $w = 2.3$ cm, $t = 2.4$ cm (Fig. 16(a)), in ambient	5.1	532	260	166	3.6	1.3
Covered with fiberglass insulation of size $l = 4$ cm, $w = 2.3$ cm, $t = 2.4$ cm, under vacuum	2.8	414	260	186	1.3	1.3
Placed in insulation of size $l = 10$ cm, $w = 8$ cm, $t = 8$ cm (Fig. 16(b)), in ambient	2.5	411	260	181	1.3	1.0
Placed in 10 cm × 8 cm × 8 cm insulation, under vacuum	1.8	386	260	181	0.6	1.0

The convective loss shown here actually accounts for the combined effect of air conduction and natural convection losses.

off on the amount of insulation that can be used without adding much to the weight and volume of the integrated system. Additionally, it would be helpful to use a low-*k* gas like argon instead of air surrounding the integrated device to reduce gas conduction losses. We observed that the use of vacuum below 50 mTorr reduces these losses by at least 60%. However, at this level of vacuum, the air conduction and convection could not be entirely suppressed. This is consistent with other reports in literature [17,19]. Vacuum packaged insulation is superior for reducing these heat losses without significantly increasing volume. However, it seems that a vacuum down to 10^{-4} Torr or below is required to minimize losses through the ambient air [17]. This presents a challenge in developing a reliable and hermetic vacuum package that can hold such a low pressure for a long period of time. We suggest employing the combination of low-*k* insulating material and vacuum packaging to reduce air conduction and convective losses.

- Radiative heat losses from a free surface can be reduced by using reflective insulation or by employing high reflectivity and low emissivity materials.

We observed that heat loss to the ambient via gas conduction, convection, and radiation was substantial compared to the required heat for critical energy-consuming fuel processing functions including fuel vaporization and the endothermic SR reaction. Considering the integrated device of the vaporizer, combustor, SR, and PrOx having a size of 1 cm × 1 cm × 0.5 cm, if we employ the above packaging recommendations, it would still result in a minimum heat loss of 1.0 W. The total energy required considering heat loss (1.0 W) plus energy to drive the endothermic SR reaction (0.13 W) and fuel and water vaporization (0.20 W) is then 1.33 W. Considering 75% hydrogen utilization in the fuel cell, hydrogen recycled from the fuel cell anode when burned gives only 0.38 W, thus an additional of 1.33 − 0.38 = 0.95 W would required by combusting methanol fuel. The device can produce 3.84e−4 mol min^{-1} of hydrogen, resulting in a lower heating value of 1.55 W, while considering fuel cell efficiency as mentioned previously it can produce a net 0.65 W output. Thus, we can see that we will begin to see the benefits of an integrated fuel processor + fuel cell approach as systems are designed for powers exceeding a few W. Fig. 16 shows the anticipated heat loss after stacking of reactor layers and employing packaging recommendations, including the heat duty required for the endothermic SR reaction and for fuel and water vaporization, and the LHV of un-utilized hydrogen available at different power outputs of 1, 10, and 20 W from the fuel cell.

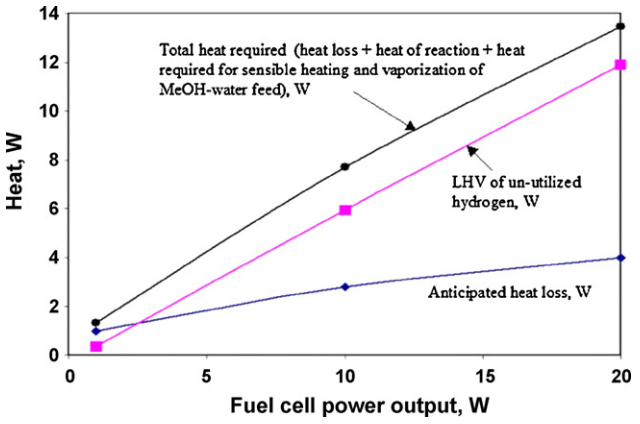

Fig. 16. Anticipated heat loss, reformer energy requirement, and LHV of the un-utilized hydrogen in the anode off-gas as a function of fuel cell power output.

5. Conclusion

Understanding thermal management issues in a microscale fuel processor is crucial in order to reduce heat losses and improve thermal efficiency. This work was aimed to understand this critical issue and develop a knowledge base required to rationally design and integrate the microchemical components of a fuel processor. A silicon microreactor-based steam reformer was successfully designed, fabricated, and demonstrated in the context of complete thermal integration as determined from the thermal simulation for the integrated system. The fabricated model components of an integrated device were used for the acquisition of critical thermal parameters of the overall coefficients for the transfer of heat from components to one another and to the outside environment by different heat loss pathways. Based on thermal characterization experiments, the heat loss mechanisms and heat coefficients were determined and suggestions were made for scale up and implementation of packaging schemes to reduce different modes of heat losses. Acquisition of the thermal experimental data help to verify and improve the model used to simulate thermal behavior of an integrated device. This combined experimental/modeling approach can then be used as the quantitative basis for designing an integrated portable fuel processor.

The SR microreactor produced 14.3 sccm of hydrogen (corresponding to a net power output of 1.04 W from the fuel cell) with relatively low levels of carbon monoxide. The experiments effectively demonstrated the potential of microreactor-based on-demand H_2 generation, and provide impetus for a subsequent phase of development involving completely integrated subsystems.

Acknowledgements

The financial support from the Picatinny TACOM/ARDEC and New Jersey Commission of Science and Technology (NJCST). The authors would like to thank Mike Skvarla and Rob Ilic of Cornell NanoScale Science and Technology Facility (CNF) for their generous support and technical assistance during the microfabrication of the integrated device.

The silicon and glass microfabrication was performed in part at the Cornell NanoScale Facility (a member of the National Nanofabrication Users Network) which is supported by the National Science Foundation under Grant ECS-9731293, Cornell University and industrial affiliates.

References

[1] Fuel Cell Handbook, fifth ed., Report prepared by EG&G Services for the US Department of Energy, National Energy Laboratory, 2000.

[2] K. Kordesch, G. Simader, Fuel Cells and Their Applications, VCH, Germany, 1996.
[3] C. Song, Catal. Today 77 (2002) 17–49.
[4] A.Y. Tonkovich, J.L. Zilka, M.J. LaMont, Y. Wang, R.S. Wegeng, Chem. Eng. Sci. 54 (1999) 2947–2951.
[5] Y. Choi, H.G. Stenger, Appl. Catal. B 38 (2002) 259–269.
[6] P.J. de Wild, M.J.F.M. Verhaak, Catal. Today 60 (1) (2000) 3–10.
[7] B.A. Peppley, J.C. Amphlett, L.M. Kearns, R.F. Mann, Appl. Catal. A 179 (1999) 21–29.
[8] C.J. Jiang, D.L. Trimm, M.S. Wainwright, Appl. Catal. A 93 (1993) 245–255.
[9] W. Ehrfeld, V. Hessel, H. Lowe, Microreactors: New Technology for Modern Chemistry, Wiley-VCH, Weinheim, 2000.
[10] R.S. Besser, X. Oyuang, H. Surangalikar, Chem. Eng. Sci. 58 (2003) 19–26.
[11] K. Shah, R.S. Besser, Chem. Eng. Technol. 28 (2005) 303–313.
[12] D.J. Seo, W.L. Yoon, Y.G. Yoon, S.H. Park, G.G. Park, C.S. Kim, Electrochim. Acta 50 (2004) 719–723.
[13] J.D. Holladay, J.S. Wainright, E.O. Jones, S.R. Gano, J. Power Sources 130 (2004) 111–118.
[14] E.R. Delsman, M.H.J.M. de Croon, G.J. Kramer, P.D. Cobden, Ch. Hofmann, V. Cominos, J.C. Schouten, Chem. Eng. J. 101 (2004) 123–131.
[15] A.V. Pattekar, M.V. Kothare, J. Microelectromech. Syst. 13 (2004) 7–18.
[16] Y. Kawamura, N. Ogura, T. Yamamoto, A. Igarashi, Chem. Eng. Sci. 61 (2006) 1092–1101.
[17] L.R. Arana, S.B. Schaevitz, A.J. Franz, M.A. Schmidt, K.F. Jensen, J. Microelectromech. Syst. 12 (2003) 600–612.
[18] J.A. Hallmark, Presented at The Knowledge Science Foundation's 5th International Small Fuel Cells 2003: Small Fuel Cells for Portable Power Applications, New Orleans, LA, May 2003.
[19] T. Terazaki, M. Nomura, K. Takeyama, O. Nakamura, T. Yamamoto, J. Power Sources 145 (2005) 691–696.
[20] F.P. Incropera, D.P. Dewitt, Fundamental of Heat and Mass Transfer, fifth ed., John Wiley & Sons, NY, 2001.
[21] P. Atkins, J.D. Paula, Physical Chemistry, seventh ed, W.H. Freeman & Company, NY, 1997.
[22] C.J.M. Laasance, Electron. Cooling Mag. 8 (4) (2002), http://www.electronics-cooling.com/html/2002_november_techdata.html.
[23] A.F. Mills, Basic Heat and Mass Transfer, Prentice Hall, NJ, 1999.
[24] A. Bejan, A.D. Kraus, Heat Transfer Handbook, John Wiley & Sons, NY, 2003.
[25] I. Martorell, J. Herrero, F.X. Grau, Int. J. Heat Mass Transfer 46 (2003) 2389–2402.
[26] A. Giani, F. Mailly, R. Bonnot, F. Pascal-Delannoy, A. Foucaran, A. Boyer, Microelectron. J. 33 (2002) 619–625.